

Radar Detection of Phobos

S. J. OSTRO, R. F. JURGENS, D. K. YEOMANS, E. M. STANDISH, W. GREINER

Radar echoes from the martian satellite Phobos provide information about that object's surface properties at scales near the 3.5-cm observing wavelength. Phobos appears less rough than the moon at centimeter-to-decimeter scales. The uppermost few decimeters of the satellite's regolith have a mean bulk density within 20% of 2.0 g cm^{-3} . The radar signature of Phobos (albedo, polarization ratio, and echo spectral shape) differs from signatures measured for small, Earth-approaching objects, but resembles those of large ($\geq 100\text{-km}$), C-class, mainbelt asteroids.

THE MARTIAN MOONS, PHOBOS AND Deimos, are irregularly shaped, heavily cratered, dark-grey objects with maximum dimensions near 27 and 15 km, respectively. Discovered just 111 years ago, they are extremely difficult to study with Earth-based optical telescopes. However, from successful investigations carried out by Mariner 9 and Viking spacecraft while orbiting Mars, we know more about these objects than about any other small planetary body (1). Like Earth's moon, their surfaces appear to be blanketed by a regolith of unconsolidated, particulate material $>10 \text{ m}$ thick. The satellites' colors and visual albedos resemble those of C-class asteroids, which dominate the main asteroid belt ~ 3 astronomical units (AU) from the sun and are thought to be mineralogically similar to carbonaceous chondrites, our most primitive meteorites. Phobos and Deimos might be captured asteroids, or perhaps they formed in orbit around Mars from debris that accumulated during the planet's accretion (2). In either case, they provide our first detailed views of small planetary objects and possibly the most accessible examples of relatively primitive solar system material. These considerations, plus the potential for the satellites to serve as outposts for the human exploration of Mars (3), argue for detailed characterization of their surfaces and provide the rationale for the current Soviet spacecraft mission to Phobos.

During the exceptionally close approach of Mars to Earth in September and October 1988, we used the Goldstone 70-m antenna as a radar telescope (4) to observe Phobos. Our detection of echoes constitutes an active remote-sensing experiment on a martian moon, yields information about Phobos's near-surface structure and bulk density at

centimeter-to-decimeter scales, and establishes a valuable guide for interpreting radar signatures of asteroids and comets.

We completed a total of 117 transmit/receive cycles on five dates (Table 1). Each run consisted of transmission of a highly monochromatic, 8495-MHz (3.5-cm wavelength) signal toward Phobos for about 6.5 min (the round-trip light time) followed by reception of echoes for a similar duration. Data reduction procedures were similar to those described by Ostro *et al.* (5).

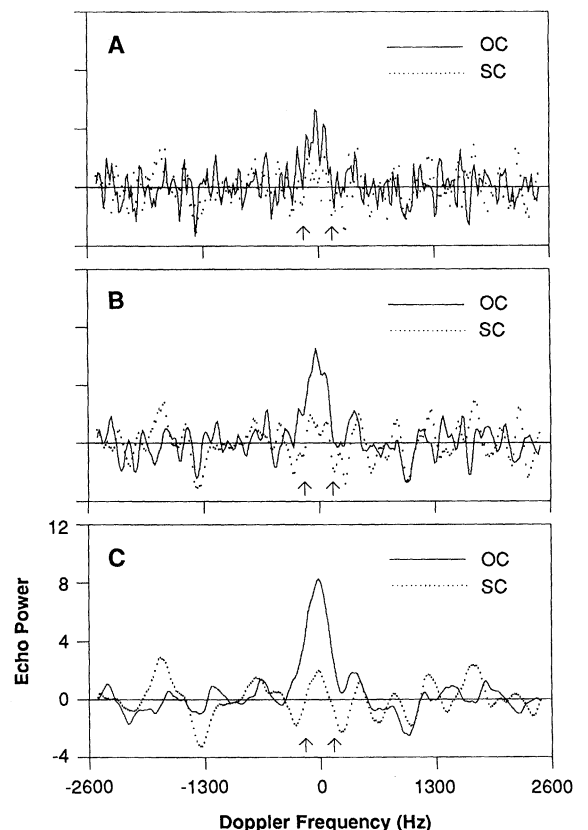
Since the 1-arc-minute halfwidth of Goldstone's antenna beam exceeded the maximum angular separation of Mars from Pho-

bos, the planet was illuminated by transmissions beamed toward Phobos and consequently returned extremely strong echoes. However, the Doppler frequencies of Mars and Phobos echoes were widely separated from each other except during Mars/Phobos conjunctions. We kept our receiver tuned to Phobos frequencies, which were predicted by a site ephemeris, and suspended data acquisition whenever any part of Mars's echo would have entered our 10-kHz passband. The orbital/rotational phase coverage of our data is complete and quite uniform (Table 1) apart from the intentional, $\sim 22^\circ$ -wide gaps at conjunctions.

Two separate receiver channels permitted simultaneous reception in the same sense of circular polarization as transmitted (the SC sense) and the opposite (OC) sense. The handedness of a circularly polarized wave flips upon normal reflection from a smooth dielectric interface, so the OC sense dominates echoes that are due primarily to single-reflection backscattering from smooth surfaces. SC echoes can arise from multiple scattering, or from single reflections from surfaces having radii of curvature within an order of magnitude of the radar wavelength. Hence, the circular polarization ratio μ_c , of SC to OC power, quantifies the severity of near-surface, wavelength-scale "roughness."

Figure 1 shows weighted sums of all our echo spectra. OC echo is present within a central band at least $\sim 200 \text{ Hz}$ wide, but any

Fig. 1. Phobos radar echo spectra (with echo power labeled in standard deviations) obtained in the OC and SC polarizations, at frequency resolutions of (A) 40, (B) 100, and (C) 250 Hz. Axes are the same for each plot. Arrows show expected locations of echo edges. Zero Doppler frequency corresponds to echoes from Phobos's center of mass, as predicted by our ephemeris. The noise samples in our spectra approximate to the expected degree a zero-mean, unit-variance, normal distribution.



Jet Propulsion Laboratory, California Institute of Technology, Pasadena, CA 91109.

Table 1. Radar observations of Phobos. Intervals between midpoints of first and last receive periods on each date are given in terms of coordinated universal time (UTC) epoch and Phobos orbital phase. Phobos rotates once every 7.65 hours in synchronism with its orbital revolution. Thus, for our purposes, the satellite's orbital phase, reckoned from superior conjunction with Mars, is the same as its rotational phase. The last two dates' observations spanned more than 360°.

Date (1988)	Number of runs	Data acquisition window	
		UTC (hh:mm)	Phase (degrees)
21 September	25	04:09–11:29	289–274
24 September	17	06:43–11:15	196– 50
25 September	24	03:45–11:09	106– 94
26 September	26	03:40–11:26	150–157
3 October	25	02:53–10:35	98–101

SC echoes are concealed by noise. From the available information about Phobos's dimensions (6) and spin vector, we know that the edge-to-edge echo bandwidth would range from ~270 Hz near Mars conjunction to ~320 Hz near elongation. Our observations sampled the maximum bandwidth configuration, but noise obscures the echo edges, whose expected positions are indicated by arrows in Fig. 1.

Our spectra yield an estimate of Phobos's circular polarization ratio: $\mu_c = 0.09 \pm 0.10$. [Calculation of the (purely statistical) standard error followed appendix I of (5); system calibration errors were practically the same for the SC and OC channels.] This result means that single reflections from smooth surface elements are the dominant source of echo, and that there is a paucity of centimeter-to-decimeter-sized particulate material within one radar penetration depth of the surface, probably a few decimeters (7).

Viking images show the surface to be rough at all scales larger than about 10 m (8). That is, large surface elements, which our echoes reveal to be smooth at scales near 3.5 cm, tend to be steeply tilted. For planetary radar targets with low μ_c , surface slope statistics are related to OC spectral shape (9). Phobos's broad OC spectrum is consistent with a wide slope distribution. Many large asteroids return echoes with low polarization ratios and broad OC spectra (10), so the topographic character of those objects might resemble that of Phobos, at least in terms of surface slope statistics.

From the OC spectrum and the Goldstone radar system's characteristics, we estimate Phobos's OC radar cross section (11): $\sigma_{oc} = 33 \pm 11 \text{ km}^2$. A common measure of radar reflectivity is the OC radar albedo, $\hat{\sigma}_{oc} = \sigma_{oc}/A_p$, with A_p the target's projected area. Using estimates of Phobos's dimensions (6) to bound the weighted average

Table 2. Subsets of Phobos data, grouped by rotational phase. Uncertainties listed for radar cross section (σ_{oc}) are standard errors attributable to receiver noise; system calibration errors should be nearly the same for each group. Values for Phobos's projected area (A_p) are derived from (6). Error in σ_{oc} propagates into estimates of albedo ($\hat{\sigma}_{oc} = \sigma_{oc}/A_p$) and bulk density (d).

Group	Phases (degrees)		σ_{oc} (km ²)	A_p (km ²)	$\hat{\sigma}_{oc}$	d (g cm ⁻³)
	Range	Average				
1	14– 57	35	7.3 ± 8.9	352	0.021 ± 0.025	0.9 ± 0.9
2	62–120	88	31.9 ± 9.0	374	0.085 ± 0.024	1.9 ± 0.3
3	126–163	144	31.9 ± 13.5	352	0.091 ± 0.038	2.0 ± 0.5
4	196–240	217	60.5 ± 9.5	353	0.171 ± 0.027	2.8 ± 0.3
5	240–300	269	34.1 ± 8.3	375	0.091 ± 0.022	2.0 ± 0.3
6	302–344	318	28.0 ± 12.4	357	0.079 ± 0.035	1.8 ± 0.5

of Phobos's projected area for our observing periods, we estimate Phobos's albedo: $\hat{\sigma}_{oc} = 0.093 \pm 0.035$.

For targets with low μ_c , $\hat{\sigma}_{oc}$ is a good first approximation to R , the Fresnel power-reflection coefficient for normal incidence (10). R depends primarily on bulk density d for porous, nonmetallic regoliths. Following Garvin *et al.* (12), we use the formula $d = 3.2 \ln[(1 + R^{1/2})/(1 - R^{1/2})]$ to obtain an estimate of Phobos's surface bulk density: $d = 2.0 \pm 0.4 \text{ g cm}^{-3}$. This result seems reasonable, given that Phobos's bodily bulk density is within 20% of 2.2 g cm^{-3} (13). Type I-II carbonaceous chondrites, whose

0.3- to 1.3- μm spectral reflectances provide an adequate match to available Phobos spectral data (14), have specific gravities ranging between 2.2 and 2.9 g cm^{-3} (15). If Phobos's surface material has a specific gravity in that interval, then our bounds on d yield an upper limit of 45% for the porosity of the top few decimeters of Phobos's regolith. Lunar soils have porosities ~45% (16), so Phobos's surface probably is at least as closely packed as the moon's.

To check for possible variations in Phobos's radar reflectivity with rotational phase, we formed weighted sums of the spectra within each of six, 60°-wide bins (Table 2).

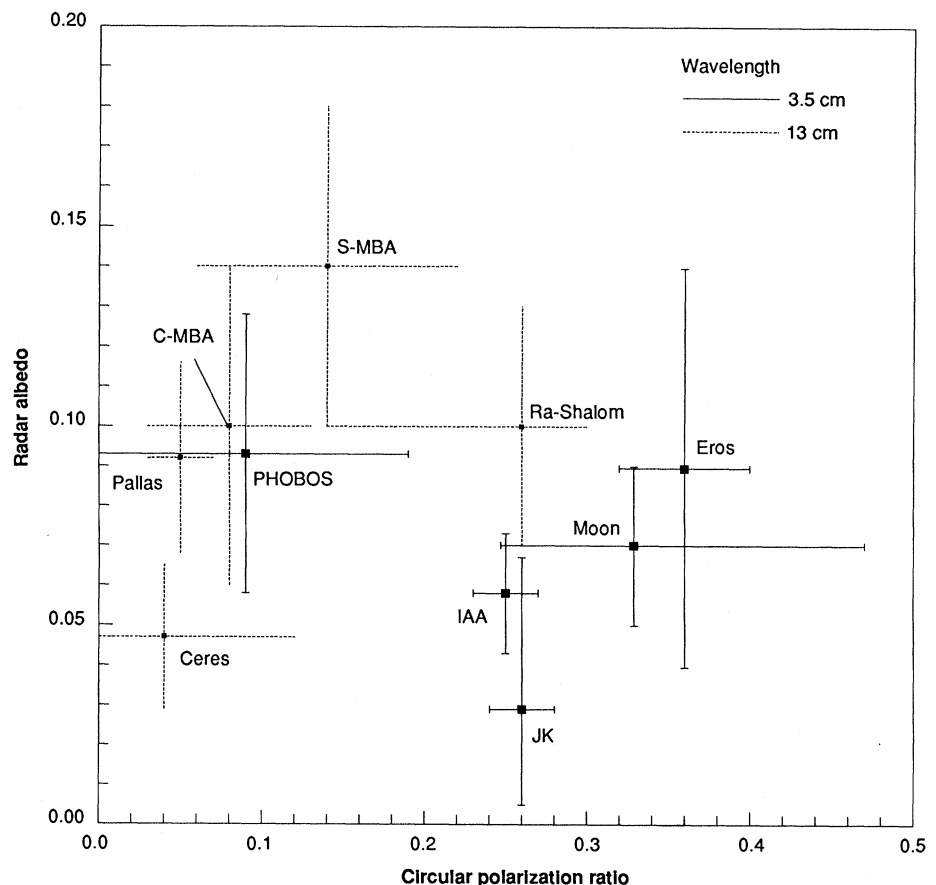


Fig. 2. Disk-integrated radar properties. JK is asteroid 1986 JK, IAA is comet IRAS-Araki-Alcock, and C-MBA and S-MBA denote the mean value and rms dispersions for C- and S-class mainbelt asteroids. See text.

Four of the groups have albedo estimates near the full-experiment average (0.093), but the first group, which covers most of the large crater Stickney and its ejecta blanket, has a lower value, while the fourth, which covers the region antipodal to Stickney, has a higher value. These variations might arise from the different distributions of large-scale (meter-to-kilometer) surface slopes for the sampled orientations of Phobos, or from regional differences in regolith bulk density (Table 2), or both.

How does Phobos's radar signature compare with those of other planetary objects, and in particular with those of C-class asteroids? Figure 2 plots 3.5-cm estimates of (μ_c , $\hat{\sigma}_{oc}$) for the moon (17–19) and three small, Earth-approaching objects: the ~1.5-km, C-class asteroid 1986 JK (20); the ~20-km, S-class asteroid 433 Eros (21); and the ~10-km nucleus of comet IRAS-Araki-Alcock (22). A 13-cm point for the ~2-km, C-class, Earth-approaching asteroid 2100 Ra-Shalom (23) is also shown. Mainbelt asteroid results are available just at 13 cm (10); we show the mean value and rms dispersions of (μ_c , $\hat{\sigma}_{oc}$) for nine large (>100-km), C-class objects and individual estimates for the two largest [1 Ceres (~930 km) and 2 Pallas (~540 km)], as well as the mean and root-mean-square values of (μ_c , $\hat{\sigma}_{oc}$) for seven large, S-class objects. Experience with objects observed at both wavelengths leads us to expect $\mu_c \sim 30\%$ to $\sim 300\%$ larger at 3.5 cm (18, 21).

In this light, Fig. 2 suggests that Phobos bears a closer resemblance to large, C-class, mainbelt asteroids than to other planetary targets. On the other hand, the moon (17) and the small, Earth-approaching bodies have larger μ_c estimates than Phobos, indicating more severe small-scale roughness. This result, as well as the variance in radar albedo (and hence in near-surface bulk density), might reflect intrinsic differences in the physical properties of surface materials or variations in regolith generating processes (1).

In summary, Phobos's surface apparently resembles those of many (if not most) large, C-class asteroids in terms of bulk density, small-scale roughness, and large-scale topographic character, but differs from the surfaces of the moon and at least some small, Earth-approaching objects. Additional 3.5-cm and 13-cm radar observations of asteroids, comets, and the martian satellites can clarify these relations.

REFERENCES AND NOTES

1. J. Veverka and J. A. Burns, *Annu. Rev. Earth Planet. Sci.* **8**, 527 (1980).
2. D. J. Stevenson, A. W. Harris, J. I. Lunine, in *Satellites*, J. A. Burns and M. S. Matthews, Eds. (Univ. of Arizona Press, Tucson, 1986), pp. 39–88.
3. J. E. Oberg, *Mission to Mars* (Stackpole Books,

Harrisburg, 1982), pp. 149–157.

4. Nominal radar system characteristics were as follows: one-way antenna gain at zenith, $107^{\circ}2$; minimum system temperature, 18 K; transmitter power, 350 kW.
5. S. J. Ostro, D. B. Campbell, I. I. Shapiro, *Astron. J.* **88**, 565 (1983).
6. Ellipsoidal approximations to Phobos's figure, tabulated by T. C. Duxbury (*Icarus*, in press), have semi-axis lengths that satisfy: $12.61 \leq a \leq 13.3$, $11.1 \leq b \leq 11.33$, and $8.6 \leq c \leq 9.3$ km.
7. M. J. Campbell and J. Ulrichs, *J. Geophys. Res.* **74**, 5867 (1969).
8. P. Thomas, J. Veverka, S. Dermott, in *Satellites*, J. A. Burns and M. S. Matthews, Eds. (Univ. of Arizona Press, Tucson, 1986), p. 831.
9. R. A. Simpson and G. L. Tyler, *IEEE Trans. Antennas Propag.* **AP-30**, 438 (1982).
10. S. J. Ostro, D. B. Campbell, I. I. Shapiro, *Science* **229**, 442 (1985).
11. The uncertainty assigned to σ_{oc} incorporates statistical error attributable to receiver noise and much larger systematic errors arising primarily from uncertainty in antenna gain and pointing accuracy.
12. J. B. Garvin, J. W. Head, G. H. Pettengill, S. H. Zisk, *J. Geophys. Res.* **90**, 6859 (1985).
13. J. A. Burns, in *Satellites*, J. A. Burns and M. S. Matthews, Eds. (Univ. of Arizona Press, Tucson, 1986), p. 14.
14. K. D. Pang et al., *Science* **199**, 64 (1978).
15. B. P. Glass, *Introduction to Planetary Geology* (Cambridge Univ. Press, Cambridge, 1982), p. 101.
16. W. D. Carrier III, J. K. Mitchell, A. Mahmood, *Proc. Lunar. Sci. Conf.* **4**, 2403 (1973).
17. Our value for the moon's μ_c ($0.33^{+0.14}_{-0.08}$) combines a 3.5-cm OC albedo of 0.07 ± 0.02 (18) with a 3.8-cm SC albedo of 0.023 ± 0.003 , derived from (19).
18. G. H. Pettengill, *Annu. Rev. Astron. Astrophys.* **16**, 265 (1978).
19. S. H. Zisk, G. H. Pettengill, G. W. Catuna, *Moon* **10**, 17 (1974), figure 10.
20. S. J. Ostro et al., *Icarus*, in press.
21. R. F. Jurgens and R. M. Goldstein, *ibid.* **28**, 1 (1976); B. Zellner, *ibid.*, p. 149. S-class asteroids are thought to be mineralogically similar to stony-iron or ordinary chondritic meteorites.
22. R. M. Goldstein, R. F. Jurgens, Z. Sekanina, *Astron. J.* **89**, 1745 (1984); Z. Sekanina, *ibid.* **95**, 1876 (1988).
23. S. J. Ostro, A. W. Harris, D. B. Campbell, I. I. Shapiro, J. W. Young, *Icarus* **60**, 391 (1984); S. J. Ostro, D. B. Campbell, I. I. Shapiro, *Bull. Amer. Astron. Soc.* **17**, 729 (1985). Most 13-cm values of μ_c for small, non-C-class, Earth-approaching objects range from 0.2 to 1.0.
24. We thank D. Choate, P. Dendrenos, C. Ellston, R. Genzmer, L. Robinett, S. Walmer, and R. Winkler for help with the observations. This research was conducted at the Jet Propulsion Laboratory, California Institute of Technology, under contract with the National Aeronautics and Space Administration.

19 January 1989; accepted 24 February 1989

Imaging Crystals, Polymers, and Processes in Water with the Atomic Force Microscope

B. DRAKE, C. B. PRATER, A. L. WEISENHORN, S. A. C. GOULD, T. R. ALBRECHT, C. F. QUATE, D. S. CANNELL, H. G. HANSMA, P. K. HANSMA

The atomic force microscope (AFM) can be used to image the surface of both conductors and nonconductors even if they are covered with water or aqueous solutions. An AFM was used that combines microfabricated cantilevers with a previously described optical lever system to monitor deflection. Images of mica demonstrate that atomic resolution is possible on rigid materials, thus opening the possibility of atomic-scale corrosion experiments on nonconductors. Images of polyaniline, an amino acid polymer, show the potential of the AFM for revealing the structure of molecules important in biology and medicine. Finally, a series of ten images of the polymerization of fibrin, the basic component of blood clots, illustrate the potential of the AFM for revealing subtle details of biological processes as they occur in real time.

THE ATOMIC FORCE MICROSCOPE (AFM) (1) gives topographic images by scanning a sharp tip over a surface (2) and has been used to produce atomic-resolution images of both conductors (3) and nonconductors (4). Its published technological applications already include atomic-scale friction measurements (5), imaging of magnetic fields above thin-film recording heads (6), imaging of polymers (7), and imaging of photoresist on silicon (8).

The images we present in this report show that the AFM can be used on a large and important class of systems: nonconductors

covered with aqueous solutions. This class includes many important systems in biology, medicine, and technology, from mitochondria in cytoplasm to painted ships in seawater. The AFM obtains images fast enough (a few seconds per image) to observe many biological and chemical processes in real time.

A new, gentler and more reliable AFM

B. Drake, C. B. Prater, A. L. Weisenhorn, S. A. C. Gould, D. S. Cannell, H. G. Hansma, P. K. Hansma, Department of Physics, University of California, Santa Barbara, CA 93106.
T. R. Albrecht and C. F. Quate, Department of Applied Physics, Stanford University, Stanford, CA 94305.